RESEARCH ARTICLE | AUGUST 14 2023

A variable stiffness method for pneumatic flexible arms

Xia Wang; Dexu Geng; He Peng; Wenzhi Xu; Dandan Wang; Lizhong Zhang

AIP Advances 13, 085316 (2023)
https://doi.org/10.1063/5.0157956

AIP Advances ARTICLE pubs.aip.org/aip/adv

A variable stiffness method for pneumatic flexible arms

Cite as: AIP Advances 13, 085316 (2023); doi: 10.1063/5.0157956
Submitted: 12 May 2023 • Accepted: 25 July 2023 •
Published Online: 14 August 2023

View Online Export Citation CrossMark

Xia Wang,[1,2,a)] Dexu Geng,[2,b)] He Peng,[2,c)] Wenzhi Xu,[2,d)] Dandan Wang,[3,e)] and Lizhong Zhang[1,f)]

AFFILIATIONS

[1] College of Mechanical and Electrical Engineering, Changchun University of Science and Technology, Changchun 130022, China
[2] College of Mechanical Engineering, Beihua University, Jilin 132021, China
[3] Changchun Institute of Optics, Fine Mechanics and Physics, Chinese Academy of Sciences, Changchun 130033, China

[a)] 869738124@qq.com
[b)] gengdx64@163.com
[c)] penghe888@126.com
[d)] 2868984633@qq.com
[e)] 1060376608@qq.com
[f)] **Author to whom correspondence should be addressed:** zlzcust@126.com

ABSTRACT

In this study, a three-degree-of-freedom pneumatic flexible arm with a braking function was designed to overcome the shortcomings of low bearing capacity and insufficient rigidity of existing flexible arms. The braking force was adjusted by controlling the air pressure entering the brake, changing the stiffness of the flexible arm, and enhancing the posture maintainability of the flexible arm. A theoretical model of the braking force and stiffness of a flexible arm was established, and applicable experiments were conducted. The theoretical data were consistent with the experimental results. The braking force linearly increased with the increase of braking pressure, at a brake air pressure of 0.40 MPa. The braking force of a single braking unit reached 276 N. The stiffness nonlinearly increased with an increase in the brake air pressure. At a brake air pressure of 0.4 MPa, the axial stiffness of the flexible arm in the initial state had the highest value of 20 kN/m. The stiffness change in the bending direction of the flexible arm in the spatial bending state was the largest and increased by 12.4 times. The proposed flexible arm exhibited high stiffness and flexible movement; thus, it can be used as a flexible arm to support other end effectors. The proposed variable stiffness method can be practically employed to maintain the posture of flexible robots, which has a high practical value.

I. INTRODUCTION

Flexible robots have broad application prospects in the military, industrial, service, medical, and other fields because of their high flexibility and ability to adapt to unstructured environments; hence, they have been widely studied and various flexible mechanisms have been proposed.[1–4] For example, inspired by the elephant trunk, the German company Festo developed a series of bionic robots based on the McKibben pneumatic artificial muscle.[5–16] Jiang *et al.* were inspired by the origami process and developed a software robotic arm based on an origami structure.[17] Jiang *et al.* developed a soft robot arm using a honeycomb pneumatic network structure that could easily complete various tasks, such as opening doors, twisting bottle caps, and pulling drawers in daily life.[18] Surgical robots for medical applications have also been developed.[19–21] Flexible robots primarily use safe and flexible elastic materials that can continuously deform. However, the low stiffness and weak load capacity of flexible robots limit their applications.

Some studies have proposed variable stiffness and brake structures to improve the stiffness of flexible robots. The variable stiffness mechanism primarily includes particle blockage, layered interference, and functional materials.[22–26] In 2010, Brown *et al.* used the particle blockage principle to fabricate a sucker-type grasping device, which was simple in structure and easy to control; however, it could only grip small objects.[27] In 2016, Li *et al.* proposed a novel passive particle interference principle to achieve a variable stiffness that did not require a vacuum source or other control methods. When the inflation pressure increased from 20 to 80 kPa, the stiffness of the soft robotic arm could be increased by more than six times its original value.[28] Kim *et al.* proposed a new type of layered interference mechanism that could realize variable stiffness. The layered interference mechanism was achieved using the friction force between the layers of film materials and controlled by a negative pressure. The structure was hollow, compact, and lightweight; hence, it could be applied in minimally invasive surgery and other fields.[29] A soft gripper based on a shape memory alloy was designed, which could achieve a stiffness adjustment range of up to 55 times.[30] In 2017, Imamura *et al.* designed a soft variable stiffness gripper based on multi-layer dielectric elastomers. Stiffness adjustment was achieved by changes in the friction force between each layer of the dielectric elastomer under the attraction of static charges. The maximum stiffness change in the soft variable stiffness gripper could reach 39.2 times the original stiffness.[31] Typical brakes are mostly used in automobiles and rigid robots;[32–34] flexible robot brakes have not been sufficiently investigated. Zheng *et al.* proposed an aerodynamic elastic spherical brake that could withstand a torque of 3 N m and solve the problem of multi-directional braking of flexible robot wrists.[35] Furthermore, Geng *et al.* designed a brake for maintaining the wrist posture, which compressed the middle brake ball through axial extension of the upper and lower brake airbags to achieve braking. The maximum axial thrust was 107 N when the brake airbags were filled with an air pressure of 0.14 MPa.[36] This method provides a large range of stiffness adjustments; however, the load-bearing capacity is insufficient. Thus, it is primarily used to adjust the stiffness of flexible arm-end effectors. However, it is not appropriate for the stiffness adjustment of flexible arms with large loads. Therefore, this study introduces a three-degrees-of-freedom (3DOF) pneumatic flexible arm with a brake that can adjust the braking force to achieve stiffness changes in the flexible arm, enabling the flexible arm to have anti-torsion and posture maintenance functions. The proposed flexible arm can be used in practical applications as it overcomes the shortcomings of existing flexible arms, such as insufficient rigidity and small bearing capacity.

II. THEORY AND DESIGN

Figure 1(a) shows a 3DOF pneumatic flexible arm that consists of a flexible actuator and flexible brake. The actuator primarily is composed of three groups of fan-shaped driving units uniformly distributed along the circumference. When the three sets of driving units have the same air pressure, the arm will elongate along the axis direction; the greater the air pressure, the greater the elongation. However, when they have different air pressures, the arm is bent within the three-dimensional (3D) space range. A composite deformation motion of axial elongation and spatial bending of the flexible arm can be achieved by controlling the air pressure in the three groups of fan-shaped driving units. The brake is connected to the actuator through an elastic cable and annular brake airbags are arranged inside the brake. After the pneumatic flexible arm reaches the set position, pressure is exerted on the brake airbags and they undergo a radial deformation. The axial and radial outer sides are limited by the brake shell, and the airbags can only expand to the radial inner side, promoting radial contraction of the fan-shaped brake pad installed inside the brake airbag. The fan-shaped brake pad contacts the brake shaft as the pressure increases, which generates a braking force. The greater the input pressure of the brake airbag, the greater the braking force. The stiffness of the flexible arm is adjusted in real-time based on the load or deformation of the flexible arm, and an arbitrary pose of the flexible arm is maintained. The effective carrying capacity of the flexible arm significantly improves, as shown in Fig. 1(b).

The stiffness of the flexible arm is anisotropic owing to the high tensile and low compressive strengths of the elastic cable. When the flexible arm is in its initial state, the brake is pressurized to hold the brake shaft, and the axial elongation and spatial bending deformation of the flexible arm are limited by the elastic cable. The flexible arm has greater stiffness in all directions because the initial state of the flexible arm is axially incompressible. When a flexible arm is axially elongated or spatially bent, the brake is pressurized to hold the brake shaft, and the elastic cables limit the axial elongation and spa-

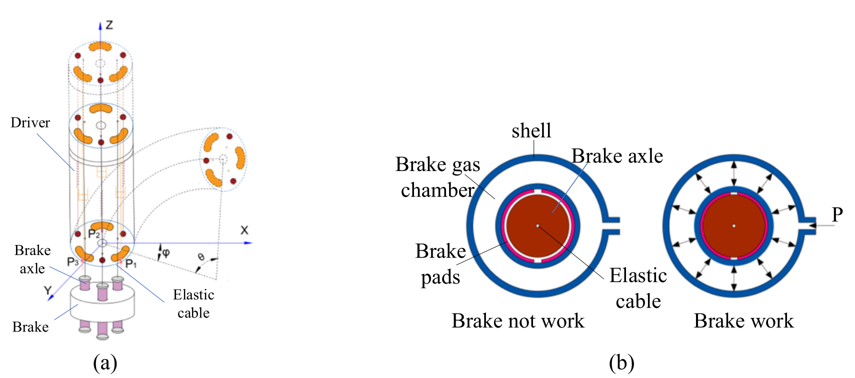

FIG. 1. Working principle of flexible arm. (a) Flexible actuator. (b) Flexible brake.

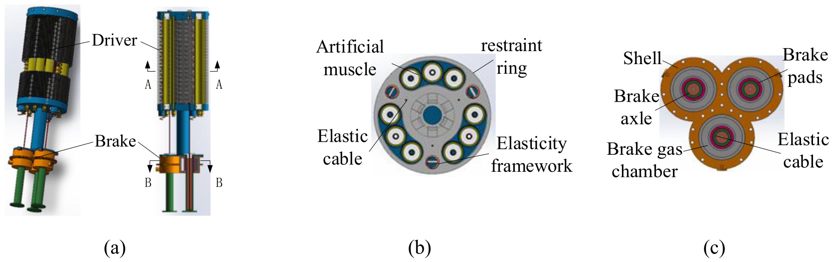

FIG. 2. Structure of flexible arm. (a) 3d model. (b) Section A-A. (c) Section B-B.

tial bending deformation of the flexible arm. However, the flexible arm is axially compressible at this time. Therefore, the flexible arm has the largest stiffness in the axial elongation direction, followed by the lateral stiffness, and the axial compression direction has the weakest stiffness. The braking pressure of the brake increases with an increase in the load or deformation displacement of the flexible arm to avoid a situation in which the flexible arm load exceeds the braking force of the brake and braking failure of the elastic cable.

The overall mass of the flexible arm is 4514.4 g, of which the mass of the actuator is 3313.3 g and that of the brake is 1201.1 g, as shown in Fig. 2(a). Table I presents the structural mass and material parameters of the flexible arm.

Figure 2(b) shows that the actuator is primarily composed of artificial muscles, elastic frameworks, elastic cables, nested restraint rings, and end covers. Several restraint rings are coaxially mounted without gaps to form three fan-shaped cavities. The nested structure of the restraint ring improves the torsional resistance of the flexible arm. Three artificial muscles are installed in each fan-shaped cavity to form a driving unit to achieve spatial bending and elongation of the flexible arm. The restraint ring limits the radial deformation of the artificial muscles without affecting the axial elongation and bending flexibility. Three elastic frameworks are evenly distributed around the circle between the three groups of fan-shaped driving units to improve the initial stiffness of the flexible arm and reset response speed. The inner ring is evenly distributed with three elastic cables connected to the brake.

The brake and upper end of the actuator are fixed by elastic cables, and three brake units of the same structure are formed by the brake airbag, fan-shaped brake pad, brake shaft, elastic cable, and brake shell, as shown in Fig. 2(c). The brake airbag is annular and made of Dragon Skin 30 liquid silicone material. A through-hole is arranged in the center to place the fan-shaped brake pad and brake shaft, and another through-hole is arranged on the side as a pressure–gas inlet. Two fan-shaped brake pads are used in each group. The brake shaft is fixed to the elastic cable in the actuator and assembled with a fan-shaped brake pad on the inner wall of the through-hole at the center of the annular airbag. The axial and radial rotations of the fan-shaped brake pad are limited by the coordination between the upper and lower shells of the brake.

TABLE I. Mass and material parameters of flexible arm.

Part name	Weight (g)	Material
Restraint ring	16.6 × 57	Nylon fiber
Actuator upper cover	595.9 × 1	Aluminum alloy
Actuator lower end cover	782.4 × 1	Aluminum alloy
Elasticity framework	59.7 × 3	65Mn
Artificial muscle	87 × 9	Silicon fluorine rubber
Brake axle	249.6 × 3	Clad metal
Brake pads	30.5 × 3	Clad metal
Brake gas chamber	34.8 × 3	Dragon skin 30
Brake shell	128.2 × 2	Aluminum alloy
Elastic cable	8.9 × 3	65Mn

III. MATHEMATICAL ANALYSIS

A. Brake force

As shown in Fig. 3, when the brake airbag is filled with a pressure gas to generate a radial expansion, it pushes the brake pad toward the center and makes contact with the brake shaft. The pressure gas is isotropic, and positive pressure is generated on the inner wall of the airbag,

$$F_b = n\mathrm{R}_b \mathrm{B} P_b, \tag{1}$$

where R_b is the inner surface radius of the airbag, B is the width of the airbag, P_b is the air pressure of the brake airbag, and n is the total central angle of the friction plate.

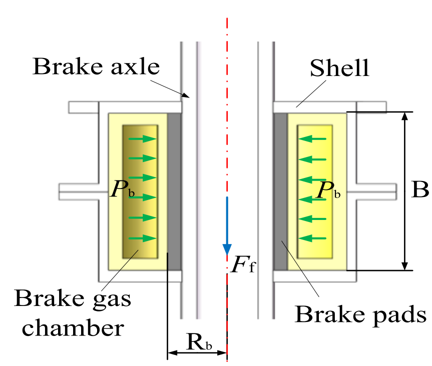

FIG. 3. Braking force analysis.

Therefore, the braking force generated between the brake disk and brake shaft is expressed as

$$F_f = \mu F_b. \quad (2)$$

B. Stiffness analysis

The flexible-arm actuator and brake are operated independently. The brake operates when the driver is in the initial state, or undergoes a deformation displacement. The braking force is adjusted to change the stiffness of the flexible arm and maintain its posture by controlling the air pressure applied to the brake. Figure 4 shows that the external loads in the directions of F_n, F_φ, and F_t are applied to the upper end of the flexible arm. The stiffness of the flexible arm in different directions is analyzed. The F_n, F_φ, and F_t directions are the axis direction, bending direction, and direction perpendicular to the bending direction of the flexible arm, respectively. In order to simplify the analysis, it is assumed that the bending deformation of the flexible arm is assumed to be circular during the flexible arm motion, the spring skeleton, elastic cable, and artificial muscle deformations are coordinated and synchronized, and the deformation impedance force of the elastic cable and friction between the elastic cable and restraint ring are small and negligible.

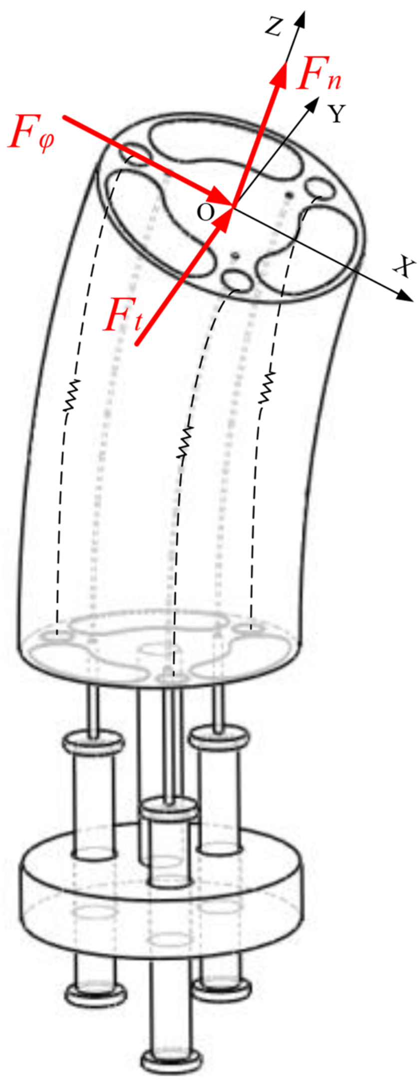

FIG. 4. External loads applied to the upper end of the flexible arm.

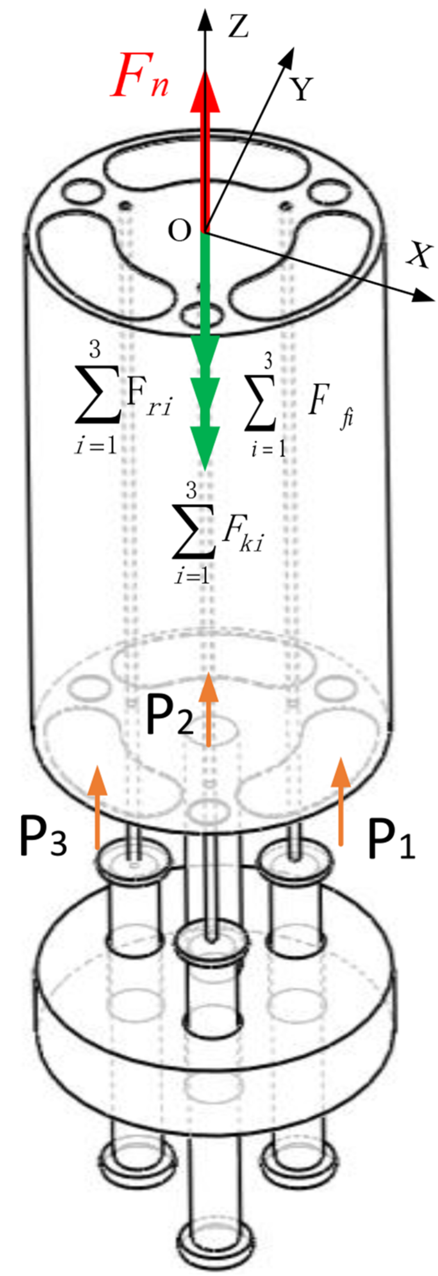

FIG. 5. Force analysis of flexible arm under the action of F_n.

1. Axial stiffness

After the initial state or deformation displacement of the flexible arm, the brake presses and locks the brake shaft to generate braking force Ff to maintain the position and posture of the flexible arm and guarantee the motion stability of the end effector. At this stage, axial force F_n is applied to the upper end of the flexible arm. Under the action of an external force, the flexible arm elongates along the axial direction, and the artificial muscle and elasticity framework generate impedance forces F_r and F_k that hinder the elongation of the flexible arm, as shown in Fig. 5.

According to the static equilibrium equation, we can write

$$F_n = \sum_{i=1}^{3} F_{ki} + \sum_{i=1}^{3} F_{ri} + \sum_{i=1}^{3} F_{fi}. \tag{3}$$

According to Hooke's law, the deformation impedance force of the elasticity framework is expressed as

$$F_{ki} = k\Delta l_n, \tag{4}$$

where k is the stiffness coefficient of the spring skeleton and Δl_n is the axial elongation of the flexible arm after being subjected to external force F_n.

According to the classical elasticity theory, the axial deformation impedance force of artificial muscles is expressed as follows:[37,38]

$$F_{ri} = \frac{3E\pi(d_1{}^2 - d_2{}^2)(l + \Delta l_i)\Delta l_n}{4(l + \Delta l_i + \Delta l_n)^2}, \tag{5}$$

where E is the elastic modulus of artificial muscle, d_1 is the outer diameter of artificial muscle, d_2 is the inner diameter of artificial muscle, l is the effective length in the initial state of actuator, and Δl_i is the elongation of the axis when the actuator reaches the specified position.

The combination of Eqs. (3)–(5) reveals that the deformation displacement of the flexible arm under the action of an external force F_n can be expressed as

$$\Delta l_n = \frac{(4F_n - 12\mu n R_b BP_b)(l + \Delta l_i)}{12k(l + \Delta l_i) + 9E\pi(d_1{}^2 - d_2{}^2) + 24\mu n R_b BP_b - 8F_n}. \tag{6}$$

The stiffness of F_n direction is expressed as follows:

$$K_n = \frac{F_n}{\Delta l_n} = \frac{F_n\left[12k(l + \Delta l_i) + 9E\pi(d_1{}^2 - d_2{}^2) + 24\mu n R_b BP_b - 8F_n\right]}{(4F_n - 12\mu n R_b BP_b)(l + \Delta l_i)}. \tag{7}$$

2. Stiffness in the bending direction

The bending condition was the same in sub-regions 1–6 due to the central symmetry of the flexible arm. When the brake is not operating, the restraint layer is regarded as the central axis. After the brake is pressurized, because the elastic cable can withstand the tension but cannot withstand the pressure, the bending direction of Zone 1 is in the range $0^\circ < \varphi \le 60^\circ$, and the restraint layer is set to pass through elastic cable No. 2. As shown in Fig. 6(a), artificial muscle P3 is elongated, P1 and P2 are compressed, elasticity framework T2 elongates, T1 and T3 are compressed, elastic cable H2 is pulled, and H1 and H3 are compressed [Fig. 6(a)].

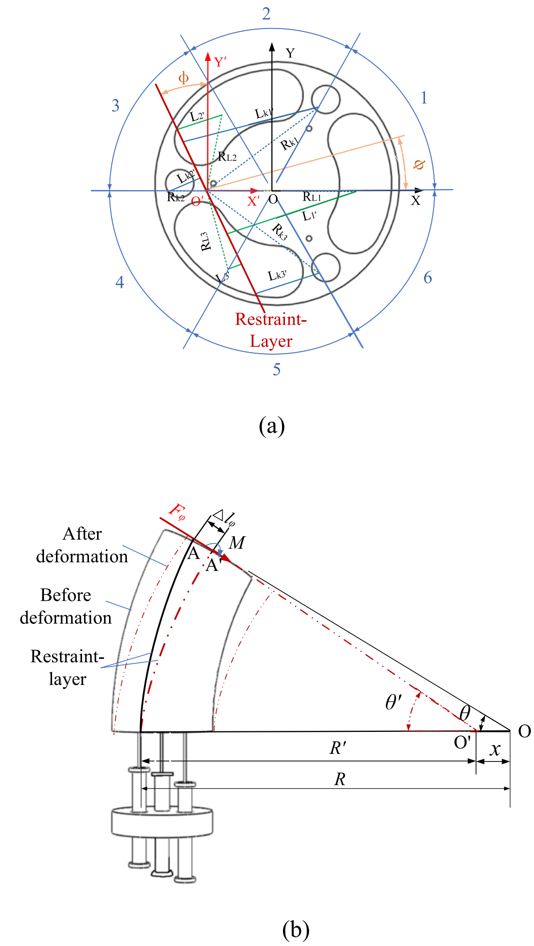

FIG. 6. Analysis of flexible arm under the action of F_φ. (a) Force arm. (b) Deformation.

As shown in Fig. 6(b), when the bending angle of the flexible arm is θ, the brake works and locks the brake shaft, and the external load F_φ is applied to the upper end of the flexible arm. The flexible arm generated a deformation along the F_φ direction, and the bending angle of the flexible arm is θ'. The air pressure in the artificial muscle remains unchanged during the process; therefore, the pressure gas and external load generate a driving moment at the upper end of the flexible arm, and the artificial muscle and elasticity framework generate an impedance moment,

$$\sum_{i=1}^{3} M_{Pi} + M_\varphi = \sum_{i=1}^{3} M_{ri} + \sum_{i=1}^{3} M_{ki}, \tag{8}$$

where M_φ is the driving moment generated by the external load F_φ.

Here,[39,40]

$$\begin{cases} \sum_{i=1}^{3} M_{Pi} = \sum_{i=1}^{3} F_{Pi}\left|L_i'\right|, \\ \sum_{i=1}^{3} M_{ri} = \sum_{i=1}^{3} \dfrac{E\pi(d_1^2 - d_2^2)\left[(d_1^2 + d_2^2)l^2 + 2d_1^2 l \Delta l'_{\theta i}\right]}{64(l + \Delta l'_{\theta i})^3} + \sum_{i=1}^{3} 3F_{ri}\left|L_i'\right|, \\ \sum_{i=1}^{3} M_{ki} = 3\left(\dfrac{E_k d^4}{32Dn(2+\mu)}\theta' + M_0\right) + \sum_{i=1}^{3} k\left|\Delta l'_{\theta ki} \cdot L'_{ki}\right| \\ M_\varphi = F_\varphi L_\varphi, \end{cases} \tag{9}$$

where L_i' is the distance from i sets of driving unit to the restraint layer after applying F_φ, θ' is the bending angle of the flexible arm under the external force F_φ, $\Delta l'_{\theta i}$ is the artificial muscle elongation when the bending angle of the flexible arm is θ', $\Delta l'_{\theta ki}$ is the elasticity framework elongation of the flexible arm at the bending angle θ', L_{ki} is the distance from the elasticity framework to the restraint layer, and L_φ is the distance from the restraint layer to the center of the upper end of the flexible arm.

The combination of Eqs. (8) and (9) reveals that air pressure P_i is applied to the three groups of driving units, and the brake operates. The bending angle of the flexible arm under the external load F_φ is expressed as

$$\begin{aligned} f(F_\varphi, P_i, \theta) = {} & \sum_{i=1}^{3} F_{Pi}\left|L_i'\right| + F_\varphi L_\varphi - \sum_{i=1}^{3} 3F_{ri}\left|L_i'\right| \\ & - \sum_{i=1}^{3} \frac{E\pi(d_1^2 - d_2^2)\left[(d_1^2 + d_2^2)l^2 + 2d_1^2 l \Delta l'_{\theta i}\right]}{64(l + \Delta l'_{\theta i})^3} \\ & - 3M_0 - \frac{E_k d^4}{32Dn(2+\mu)}\theta' - \sum_{i=1}^{3} k\left|\Delta l'_{\theta ki} \cdot L'_{ki}\right|. \end{aligned} \tag{10}$$

Here, $0^\circ < \varphi \le 60^\circ$,

$$\begin{cases} L_1{}' = -R_{L1}\cos\varphi, \\ L_2{}' = -R_{L2}\sin(\varphi + \pi/12), \\ L_3{}' = -R_{L3}\sin(\varphi - \pi/12), \end{cases}$$

$$\begin{cases} L_{k1}{}' = -R_{k1}\sin(\varphi + 53\pi/180), \\ L_{k2}{}' = R_{k2}\cos\varphi, \\ L_{k3}{}' = -R_{k3}\sin(53\pi/180 - \varphi). \end{cases}$$

According to the deformation coordination equation of the flexible arm,

$$\begin{cases} \Delta l'_{\theta i} = \Delta l_i + L'_i\theta', \\ \Delta l'_{\theta ki} = \Delta l_i + L_{ki}{}'\theta'. \end{cases} \tag{11}$$

According to the sine theorem of $\Delta A'O'O$,

$$\frac{\sin(\theta' - \theta)}{x} = \frac{\sin(\pi - \theta')}{R - \Delta l_\varphi}, \tag{12}$$

$$(R - x)\theta' = R\theta. \tag{13}$$

The combination of Eqs. (10)–(13) reveals that the stiffness of the flexible arm in the F_φ direction in Zone 1 is obtained as follows:

$$K_t = \frac{F_\varphi}{\Delta l_\varphi} = \frac{F_\varphi \sin\theta}{R\sin\theta' - R'\sin(\pi - \theta')}. \tag{14}$$

3. Stiffness in the vertical bending direction

When the bending angle of the flexible arm is θ, the brake operates and an external load F_t is applied to the upper end of the flexible arm. The flexible arm produces an additional bending deformation along the F_t direction, and the angle is θ'', as shown in Fig. 7(a). Under the action of an external load, the restraint layer changes and passes through elastic cable No. 3, as shown in Fig. 7(b).

According to the bending moment equilibrium equation,

$$\sum_{i=1}^{3} M_{Pi} + M_t = \sum_{i=1}^{3} M_{ri} + \sum_{i=1}^{3} M_{ki}, \tag{15}$$

where M_t is the driving moment generated by the external load F_t at the end cover,

$$\begin{cases} \sum_{i=1}^{3} M_{Pi} = \sum_{i=1}^{3} F_{Pi}\left|L''_i\right|, \\ \sum_{i}^{3} M_{ri} = \sum_{i=1}^{3} \dfrac{E\pi(d_1^2 - d_2^2)\left[(d_1^2 + d_2^2)l^2 + 2d_1^2 l \Delta l''_{\theta i}\right]}{64(l + \Delta l''_{\theta i})^3} + \sum_{i=1}^{3} 3F_{ri}\left|L''_i\right|, \\ \sum_{i=1}^{3} M_{ki} = 3\dfrac{E_k d^4}{32Dn(2+\mu)}\theta'' + \sum_{i=1}^{3} k\left|\Delta l''_\varphi \cdot L''_{ki}\right| \\ M_t = F_t L_t, \end{cases} \tag{16}$$

where L''_i is the distance between i sets of driving units and restraint layer after F_t is applied, θ'' is the bending angle of the flexible arm

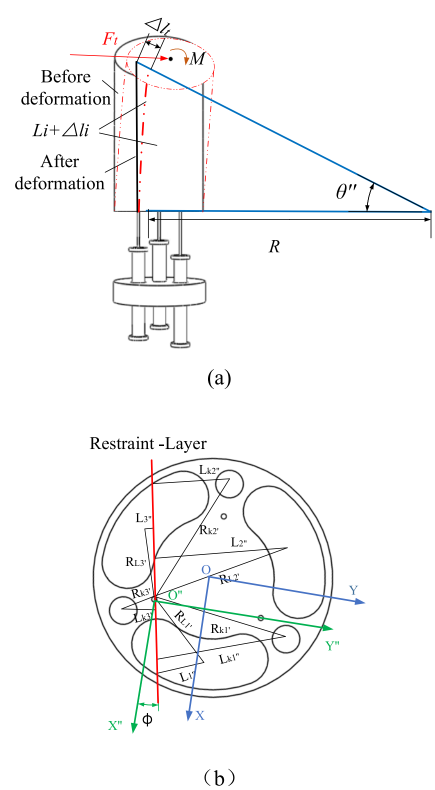

FIG. 7. Analysis of flexible arm under the action of F_t. (a) Force arm. (b) Deformation.

under the external force F_t, $\Delta l''_{\theta i}$ is the elongation of artificial muscle when the bending angle of the flexible arm is θ'', $\Delta l''_{\theta ki}$ is the elasticity framework elongation when the bending angle of the flexible arm is θ'', L''_{ki} is the distance from the elasticity framework to the restraint layer, and L_t is the distance from the upper center of the flexible arm to the lower cover.

The combination of Eqs. (15) and (16) reveals that air pressure P_i is applied to the three groups of driving units, and the brake was operating. The bending angle of the flexible arm under an external load F_t is expressed as

$$f(F_t, P_i, \theta) = \sum_{i=1}^{3} F_{Pi}\left|L''_i\right| + F_\varphi L_\varphi - \sum_{i=1}^{3} 3F_{ri}\left|L''_i\right| - \sum_{i=1}^{3} \frac{E\pi(d_1^2 - d_2^2)\left[(d_1^2 + d_2^2)l^2 + 2d_1^2 l\Delta l''_{\theta i}\right]}{64(l + \Delta l'_{\theta i})^3} - 3M_0 - \frac{E_k d^4}{32Dn(2+\mu)}\theta'' - \sum_{i=1}^{3} k\left|\Delta l''_{\theta ki} \cdot L''_{ki}\right|. \quad (17)$$

Here, $0^\circ < \varphi \le 60^\circ$,

$$\begin{cases} L''_1 = -R'_{L1} \sin(\varphi + \pi/12), \\ L''_2 = -R'_{L2} \cos\varphi, \\ L''_3 = -R'_{L3} \sin(\varphi - \pi/12), \end{cases}$$

$$\begin{cases} L''_{k1} = -R'_{k1} \sin(\varphi + 53\pi/180), \\ L''_{k2} = -R'_{k2} \sin(53\pi/180 - \varphi), \\ L''_{k3} = R_{k3} \cos\varphi. \end{cases}$$

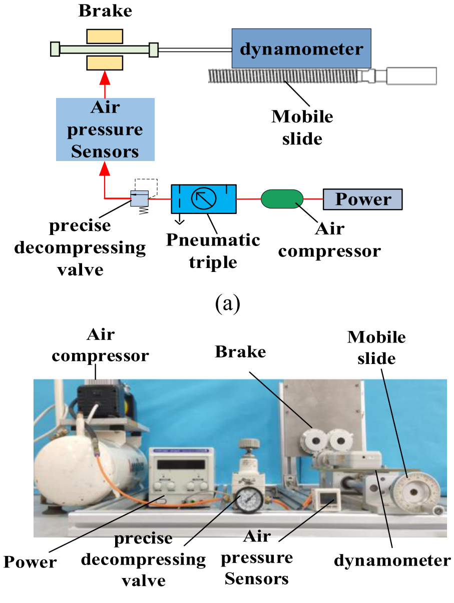

FIG. 8. Experimental principle and device of brake force. (a) Test principle. (b) Test device.

According to the bending moment equilibrium equation,

$$\begin{cases} \Delta l''_{\theta i} = \Delta l_i + L''_i\theta, \\ \Delta l''_{\theta ki} = \Delta l_i + L''_{ki}\theta. \end{cases} \quad (18)$$

According to the geometric relationship of $\Delta O''A''B''$ and illustration in Fig. 8(a),

$$\sin\theta'' = \frac{L_i + \Delta l_i}{\Delta l_t + R}. \quad (19)$$

The combination of Eqs. (17)–(19) reveals that the stiffness of the flexible arm in the F_t direction in Zone 1 is obtained as follows:

$$K_t = \frac{F_t}{\Delta l_t} = \frac{F_t \sin\theta}{L_i + \Delta l_i - R\sin\theta''}. \quad (20)$$

IV. EXPERIMENTAL ANALYSIS

The better the braking performance of the flexible arm, the higher the bearing capacity, and the better the output stability. The performance experiments were conducted using various experimental devices. The braking force and stiffness in the F_n, F_φ, and F_t directions were tested. The accuracy of the theoretical model was verified by comparing the experimental data with the theoretical analysis results, which provided a basis for the development of flexible arms.

A. Brake force experiment

Figure 8 shows the experimental principle and device used for the braking force test. The experimental device is composed of an air compressor, power, precision decompressing valve, air pressure sensor, dynamometer, and mobile slide. The dynamometer is fixed on the mobile slide, and the mobile slide pushes the dynamometer to slip along the axial direction of the brake to obtain the braking force under different air pressures. The three brake units have the same structure and only the braking force of one brake unit is tested. During the experiment, the pressure range of the brake airbag is in the range of 0–0.4 MPa, and the pressure interval increment is 0.05 MPa.

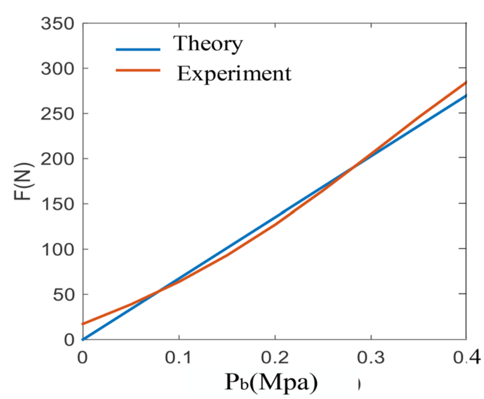

FIG. 9. Theoretical and experimental results of brake force.

The average value of five experiments is used to obtain the braking force of one brake unit under different pressures.

Figure 9 shows that the braking force linearly increases with an increase in the air pressure. When the air pressure is 0.4 MPa, the braking force of a single braking unit reaches 276 N. The experimental results were consistent with the theoretical analysis results. The error between the experimental data and theoretical analysis results was 1.73%, which verified the correctness of the theoretical model and feasibility of the brake structure.

B. Stiffness experiment

Figure 10 shows the experimental principle and device used to test the stiffness characteristics of the proposed flexible arm. The flexible arm is fixed to a turning disk located on a fixed plate, and the fixed disk is fixed on a working table. The turning disk is equipped with locating and threaded connection holes; it is used to realize the rotation of the flexible arm on the fixed disk to conveniently measure the deformation displacement of the flexible arm in different bending directions. The experimental system uses a pulley group to guarantee the accuracy of deformation-displacement measurements. The rope is connected to the upper end of the flexible arm and dynamometer through the pulley group. During the experiment, the position of the pulley group is changed in real-time by

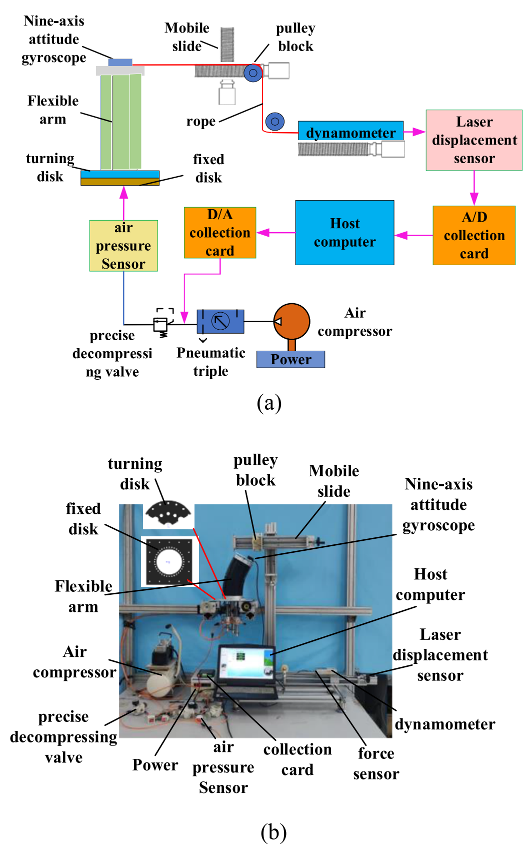

FIG. 10. Experimental principle and device of stiffness. (a) Test principle. (b) Test device.

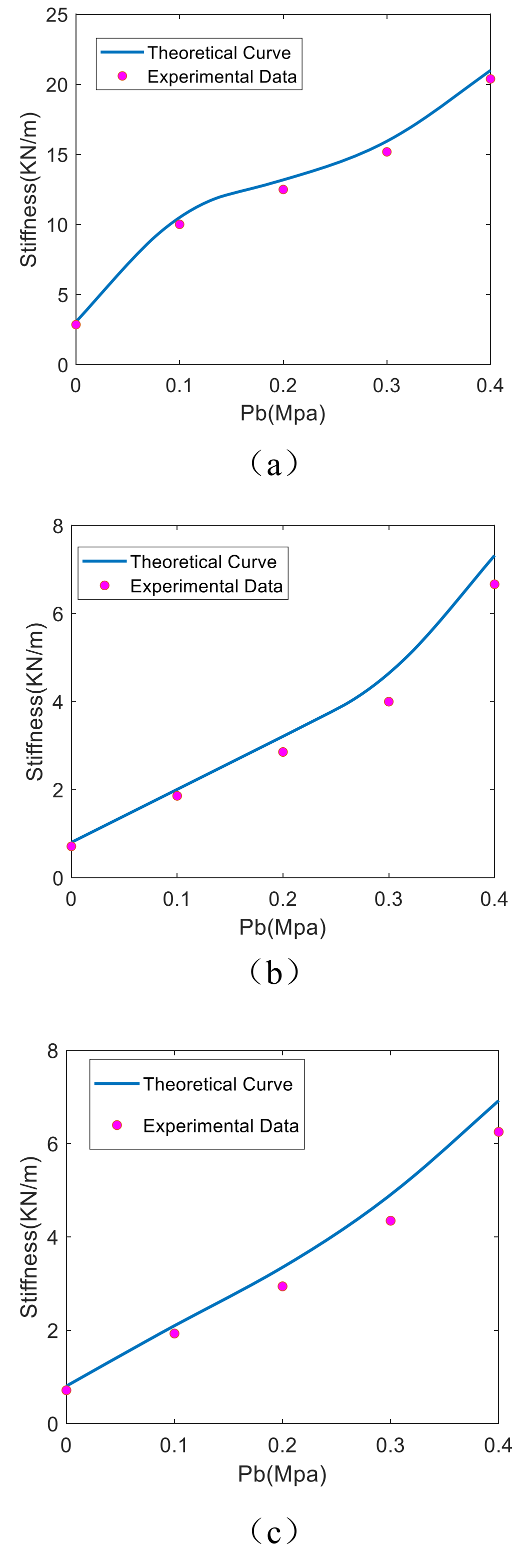

FIG. 11. Stiffness of flexible arm in the initial state. (a) F_n direction. (b) F_φ direction. (c) F_t direction.

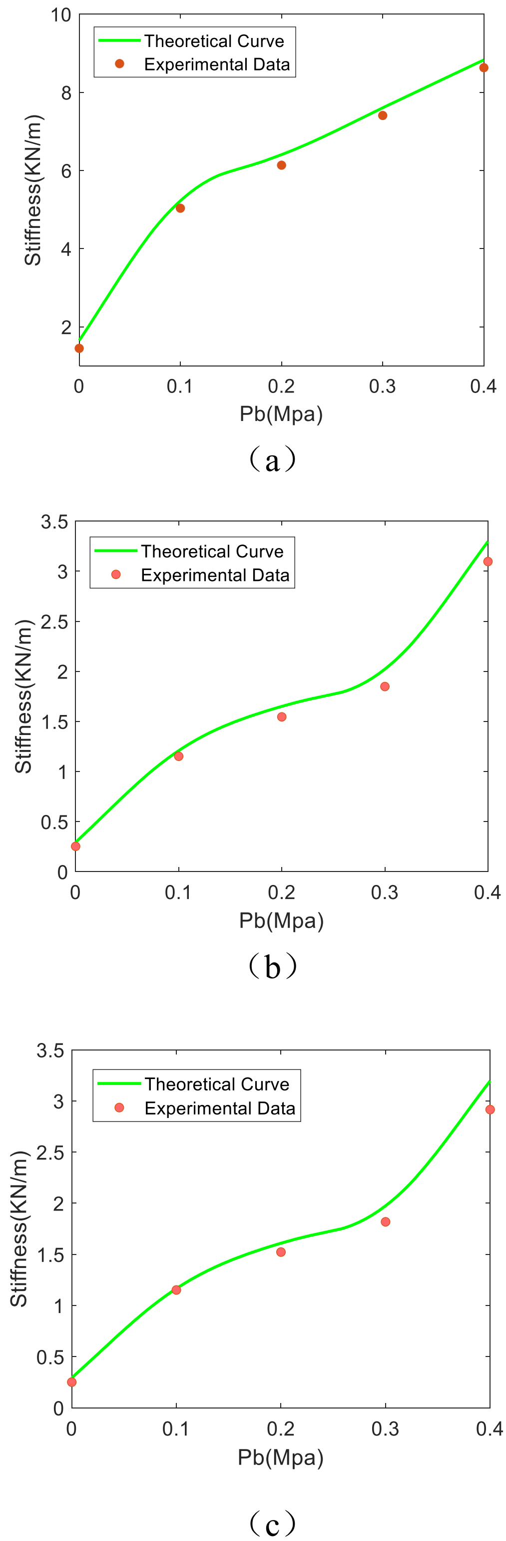

FIG. 12. Stiffness of flexible arm in the space bending state. (a) F_n direction. (b) F_φ direction. (c) F_t direction.

moving the mobile slide to confirm that the pull direction of the dynamometer is always parallel to the upper end of the flexible arm. The dynamometer is controlled to apply a fixed external force to the flexible arm in different directions. The laser displacement sensor measures the deformation of the flexible arm under an external

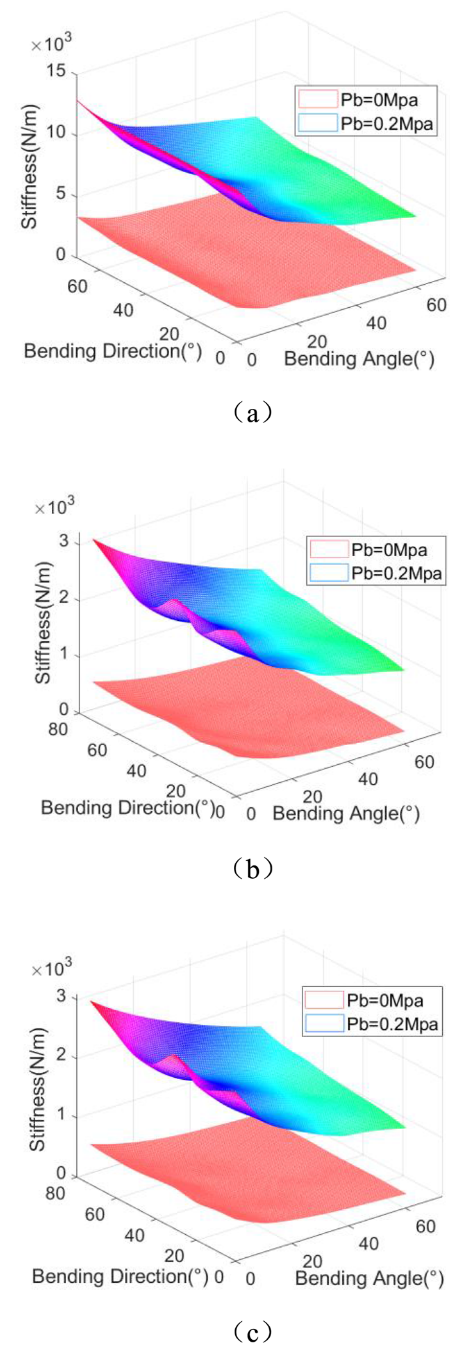

FIG. 13. Stiffness in different bending states. (a) F_n direction. (b) F_φ direction. (c) F_t direction.

load. The acquisition card transmits the collected displacement data to the host computer. The experimental data are processed to obtain the stiffness values of the flexible arm in different directions under different states.

1. Stiffness of flexible arm in the initial state

When the flexible arm is in the initial state, the brake is put into the air pressure in the range of 0–0.4 MPa, where the interval increment is 0.1 MPa. The relationship between the stiffness and braking pressure is obtained. Figure 11 shows that the experimental data and corresponding theoretical results are consistent, verifying the correctness of the proposed theoretical model. When the braking pressure is 0.4 MPa, the stiffness of the flexible arm in the F_n, F_φ, and F_t directions is 20, 6.7, and 6.3 kN/m, respectively; thus, it increases by 7.1, 9.3, and 8.8 times, respectively. In the initial state, the stiffness of the flexible arm nonlinearly increases with an increase in the braking pressure. Under the same braking pressure, the stiffness of the flexible arm in the F_n direction is higher than that in the F_φ and F_t directions, and the braking effect is better.

2. Stiffness of flexible arm in the space bending state

The flexible arm is spatially bent when pressurized. When the bending direction is 0° and the bending angle is 70°, the brake is forced into the air pressure in the range of 0–0.4 MPa, where the interval increment is 0.1 MPa. Figure 12 shows that when the braking pressure is 0.4 MPa, the stiffness of the flexible arm in the F_n, F_φ, and F_t directions is 8.6, 3.1, and 2.9 kN/m, respectively; thus, it increases by 6.1, 12.4, and 11.6 times, respectively. In the space-bending state, the stiffness of the flexible arm nonlinearly increases with an increase in the braking pressure. Under the same braking pressure, the stiffness of the flexible arm in the F_n direction is higher than that in the F_φ and F_t directions. However, the stiffness in the three directions is lower than that in the initial state, primarily because the stiffness of the flexible arm decreased with an increased deformation.

The stiffness of the flexible arm in different bending states is tested at a constant braking pressure. Seven marker points are set at equal angles in Zone 1 of the flexible arm; the bending direction is in the range 0°–60° and the air pressure of the three groups of driving units is controlled to bend the flexible arm in the corresponding direction to the seven marker points. Three external loads of F_n, F_φ, and F_t are applied to the upper end of the flexible arm to test its stiffness in different bending angles and directions. During the experiment, the braking pressure changes between 0 and 0.20 MPa, the bending angle is in the range of 0°–70°, the interval increment is 10°, and the average value is determined using five measurement results.

Figure 13 shows that when the braking pressure is constant, the bending direction slightly affects the stiffness of the flexible arm, whereas the bending angle exhibits a significant influence. The larger the bending angle, the smaller is the stiffness; thus, the stiffness of the flexible arm decreases with an increase in deformation.

3. Stiffness of flexible arm in elongating state

The flexible arm is elongated when pressurized. At a phase angle of 0° and an elongation of 30 mm, the brake is introduced into the air pressure in the range of 0–0.4 MPa, where the interval incre-

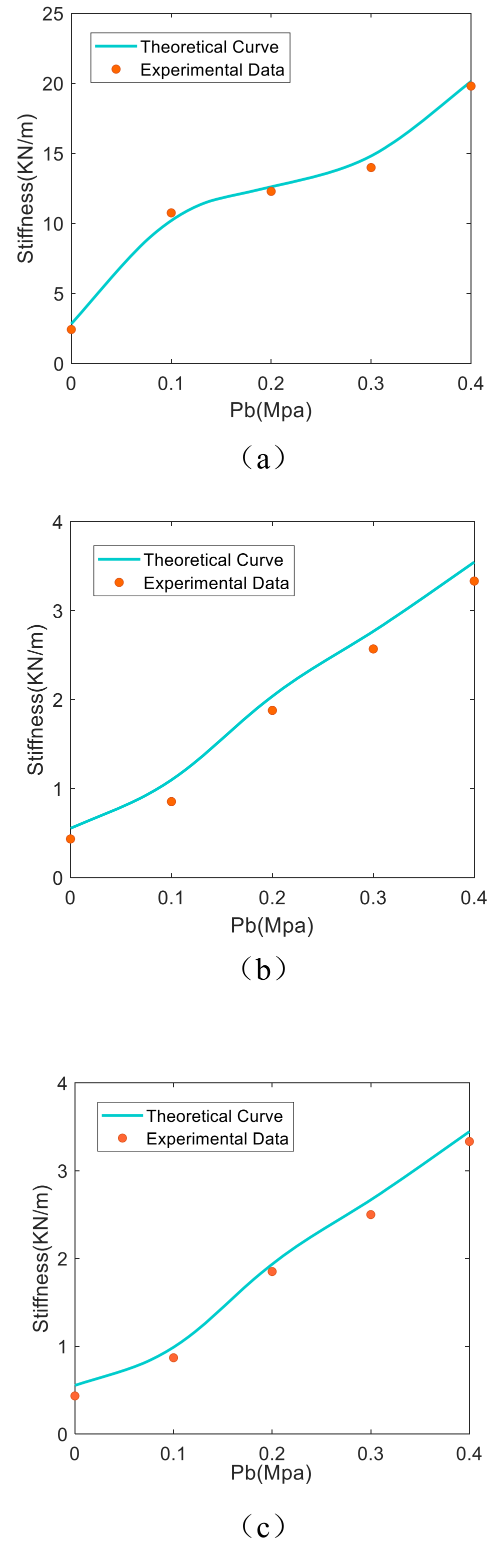

FIG. 14. Stiffness of flexible arm in elongating state. (a) F_n direction. (b) F_φ direction. (c) F_t direction.

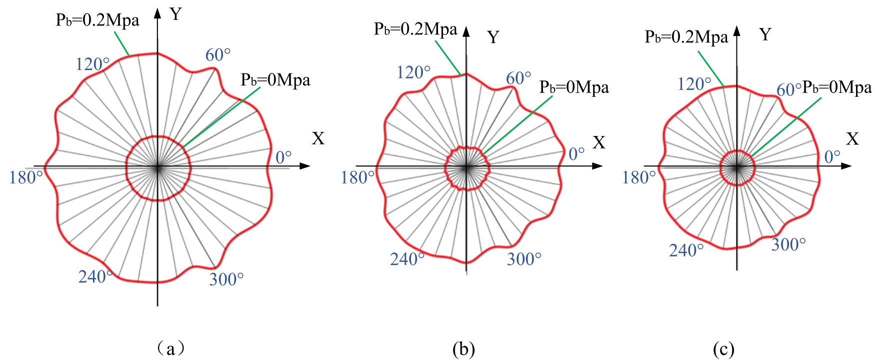

FIG. 15. Stiffness in different elongating states. (a) Δl = 0 mm. (b) Δl = 20 mm. (c) Δl = 40 mm.

ment is 0.1 MPa. Figure 14 shows that when the braking pressure is 0.4 MPa, the stiffness of the flexible arm in the F_n, F_φ, and F_t directions is 19.8, 3.3, and 3.3 kN/m, respectively; thus, it increases by 8.2, 8.3, and 8.3 times, respectively. In the elongation state, the stiffness of the flexible arm nonlinearly increases with an increase in the braking pressure. Under the same braking pressure, the stiffness of the flexible arm in the F_n direction is higher than that in the F_φ and F_t directions. The stiffness in the F_n direction in the elongation state of the flexible arm is not significantly different from that in the initial state. The stiffness in the F_φ and F_t directions is less than the corresponding stiffness in the initial state because the tensile strength of the elastic cable is high, and the compressive and flexural strengths are low. Therefore, the axial stiffness of the flexible arm in the initial and elongation states is high, and the lateral stiffness is low.

When the braking pressure is constant, the stiffness of the flexible arm in the three directions under the elongation state is tested. Over the entire circumferential range of the flexible arm, the marking points are set at equal angles and the angle increment is 10°. The three groups of driving units of the flexible arm are subjected to the same air pressure such that it is elongated along the axial direction, and the brake is pressurized. An external force is applied along the direction of the marker point to the flexible arm, and its stiffness in different directions under the elongation state is measured. During the experiment, the elongation is in the range of 0–40 mm, the interval increment is 20 mm, the braking pressure changes between 0 and 0.20 MPa, and the average value is determined using five measurement results.

Figure 15 shows the stiffness of the flexible arm in different directions in the elongation state. It can be observed that the stiffness is anisotropic. When the phase angles are 60°, 180°, and 300°,

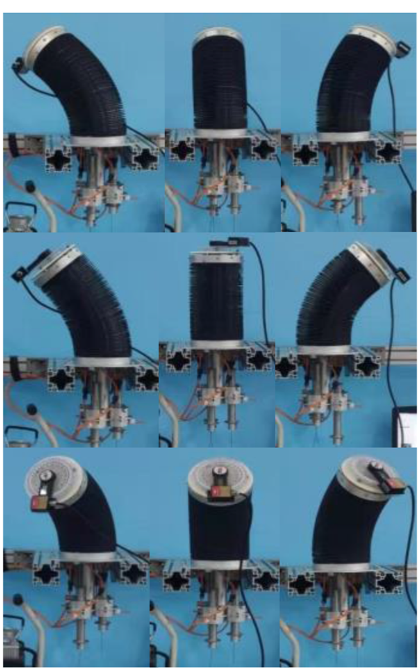

FIG. 16. Space state of flexible arm.

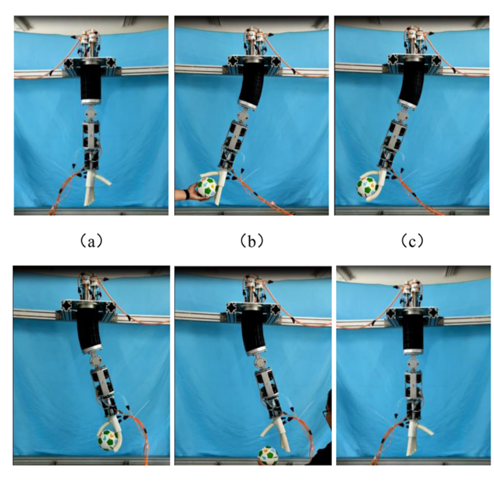

FIG. 17. Ball handling. (a) Initial state. (b) Prepare to grab. (c) Grab the ball. (d) Moving the ball. (e) Put the ball down. (f) Reset.

TABLE II. Mass and material parameters of flexible arm.

Part name	Weight (g)
Flexible arm	4593
Flexible forearm	1636.7
Flexible wrist	705.2
Flexible hand	570.5
Connector	575.1
Ball	214
Water bottle	612

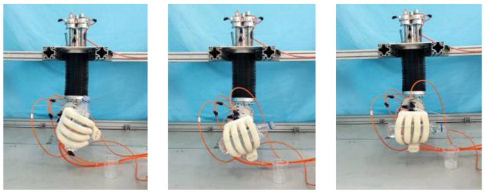

FIG. 18. Pour water. (a) Grab the water bottle. (b) Prepare to pour. (c) Pour the water.

the stiffness change curve significantly fluctuates because the stiffness of the flexible arm is affected by the position distribution of the elastic cable. Under the same braking pressure, the larger the elongation of the flexible arm, the smaller the stiffness; thus, the larger the deformation, the smaller the stiffness.

C. Motion performance experiment

The combined motion of the flexible arm in a 3D space is realized by adjusting the air pressure of the three driving units to verify the performance of the proposed flexible arm in the working process under the no-load state, as shown in Fig. 16.

In addition, a load experiment is conducted with other joints, including the flexible arm, wrist, and five-finger hand, to test the load capacity and motion characteristics under the load state. The flexible arm is used for dribbling, as shown in Fig. 17. The position of the ball is determined, the flexible arm is controlled to move to the position, the flexible five-finger hand is forced into the air pressure to grasp, the ball is transported to the set position after determining the stability of the grasp, and the five-finger hand releases the ball. The joint parameters are listed in Table II.

The flexible arm is used to pour water, as shown in Fig. 18. It grabs the water bottle and the control system controls it to pour water. During the pouring process, the flexible arm moves smoothly without any effect and no water spills out.

V. CONCLUSIONS

In this study, a 3DOF flexible pneumatic arm was designed. The brake was pressurized to hold the brake shaft. The axial elongation and spatial bending deformation of the designed flexible arm were limited by an elastic cable, and the stiffness of the flexible arm was changed to maintain its position and posture. A theoretical model of the braking force and stiffness was established, and a prototype was developed to test the braking force and stiffness. The results obtained using the theoretical model were consistent with the experimental data. The following conclusions can be drawn.

(1) The braking force linearly increased with an increase in the braking pressure. When the braking pressure was 0.40 MPa, the braking force of a single brake unit reached 276 N.
(2) In the initial state, the stiffness of the flexible arm nonlinearly increased with an increase in the braking pressure. When the braking pressure was 0.4 MPa, the stiffness in the F_n, F_φ, and F_t directions was 20, 6.7, and 6.3 kN/m, respectively; thus it increased by 7.1, 9.3, and 8.8 times, respectively. Under the same braking pressure, the stiffness of the flexible arm in the F_n direction was higher than that in the F_φ and F_t directions, and the braking effect was better.
(3) In the spatial bending state, the stiffness of the flexible arm nonlinearly increased with an increase in the braking pressure. The stiffness in the F_n, F_φ, and F_t directions was 8.6, 3.1, and 2.9 kN/m, respectively; thus, it increased by 6.1, 12.4, and 11.6 times, respectively. The stiffness in the three directions was lower than the corresponding stiffness in the initial state. When the braking pressure was constant, the stiffness of the flexible arm decreased as the bending angle increased.
(4) In the elongation state, the stiffness of the flexible arm nonlinearly increased with an increase in the braking pressure. The stiffness the F_n, F_φ, and F_t directions was 19.8, 3.3, and 3.3 kN/m, respectively; thus, it increased by 8.2, 8.3, and 8.3 times, respectively. The stiffness in the F_n direction was slightly different from that in the initial state, and the stiffness in the F_φ and F_t directions was less than the corresponding stiffness in the initial state. The stiffness of the flexible arm was anisotropic. Under the influence of the positional distribution of the elastic cable, when the phase angles were 60°, 180°, and 300°, the stiffness curve fluctuates significantly.
(5) The load experiment with other joints revealed that the designed flexible arm exhibited a large load capacity and stable motion performance.
(6) The proposed variable stiffness method for the designed pneumatic flexible arm can be used to maintain the posture of a flexible robot, which is of great significance for the development of flexible robots. The flexible arm has the largest stiffness in the axial elongation direction, followed by the lateral stiffness. The axial compression direction has the weakest stiffness, which needs to be improved in subsequent research.

ACKNOWLEDGMENTS

This work was supported, in part, by the Jilin province development and Reform Commission industry independent innovation ability (Grant No. 2020C021-4) and, in part, by the Science and Technology Research Project of the Jilin Provincial Department of Education (Grant No. JJKH20210034KJ).

AUTHOR DECLARATIONS

Conflict of Interest

The authors have no conflicts to disclose.

Author Contributions

Xia Wang: Conceptualization (equal); Writing – original draft (equal). **Dexu Geng**: Conceptualization (equal); Project administration (lead); Writing – review & editing (equal). **He Peng**: Data curation (equal); Formal analysis (equal); Software (equal). **Wenzhi Xu**: Data curation (equal); Methodology (equal); Software (equal); Writing – review & editing (equal). **Dandan Wang**: Data curation (equal); Formal analysis (equal); Methodology (equal); Software (equal); Writing – review & editing (equal). **Lizhong Zhang**: Data curation (equal); Formal analysis (equal); Methodology (equal); Software (equal); Writing – review & editing (equal).

DATA AVAILABILITY

The data that support the findings of this study are available from the corresponding author upon reasonable request.

REFERENCES

[1] Y. Gu, J. Zhou, D. Yin, and Z. Zhu, "Review of bionic soft actuators," Mech. Sci. Technol. **4**, 1–10 (2022).
[2] Q. Guo, "Research status and trend of soft robots," Rob. Technol. Appl. **3**, 13–16 (2022).
[3] Z. Liu, X. Zhang, J. Wang, Z. Wu, X. Chen, and Y. Zhao, "Design, modelling and implementation of a foldable pneumatic soft manipulator," Microgravity Sci. Technol. **34**(3), 44 (2022).
[4] Q. Hou, C. Lu, and X. Li, "A novel pose sensing model for soft manipulator based on helical FBG," Sens. Actuators, A **321**, 112586 (2021).
[5] M. Mart and S. Timo, "Mobile robot system with pneumatic gripping hand," FESTO, 2020; www.festo.com/bionics.
[6] R. Ahmad, Y. Zhang, B. Liu, M. Rubinstein Shmuel, and B. Katia, "Kirigami skins make a simple soft actuator craw," Sci. Rob. **3**(15), eaar7555 (2018).
[7] S. Nakamaru, S. Maeda, Y. Hara *et al.*, "Development of novel self-oscillating gel actuator for achievement of chemical robot," in *2009 IEEE/RSJ International Conference on Intelligent Robots and Systems* (IEEE, 2015).
[8] H. T. Lin, G. G. Leisk, and B. Trimmer, "GoQBot: A caterpillar-inspired soft-bodied rolling robot," Bioinspiration Biomimetics **6**(2), 026007 (2011).
[9] T. G. Hou, X. B. YanG, T. M. Wang *et al.*, "Locomotor transition: How squid jet from water to air," Bioinspiration Biomimetics **15**(3), 036014 (2020).
[10] M. Cianchetti, M. Calisti, L. Margheri *et al.*, "Bioinspired locomotion and grasping in water: The soft eight-arm OCTOPUS robot," Bioinspiration Biomimetics **10**(3), 035003 (2015).
[11] S. Seok, C. D. Onal, K. Cho *et al.*, "Meshworm: A peristaltic soft robot with antagoni-stic nickel titanium coil actuators," IEEE/ASME Trans. Mechatron. **18**(5), 1485–1497 (2013).
[12] C. Christianson, N. N. Goldberg, D. D. Deheyn *et al.*, "Translucent soft robots driven by frameless fluid electrode dielectric elastomer actuators," Sci. Rob. **3**(17), eaat1893 (2018).
[13] L. Wen, Z. Ren, V. Di Santo, K. Hu, T. Yuan, T. Wang, and G. V. Lauder, "Understanding fish linear acceleration using an undulatory biorobotic model with soft fluidic elastomer actuated morphing median fins," Soft Rob. **5**(4), 375 (2018).
[14] S. Afzal and C. Curran, "Design and testing of a biomimetic tuna using shape memory alloy induced propulsion," Comput. Struct. **86**(3-5), 491–499 (2007).
[15] A. D. Marchese, C. D. Onal, and D. Rus, "Autonomous soft robotic fish capable of escape maneuvers using fluidic elastomer actuators," Soft Rob. **1**(1), 75–87 (2014).
[16] H. Yang, "Design and control of flexible drive module based on shape memory alloy spring," Univeisity of Science and Technology of China, 2019.
[17] H. Jiang, X. Liu, X. Chen , "Design and simulation analysis of a soft manipulator based on honeycomb pneumatic networks," IEEE Rob. Biomimetics 350–356 (2017).
[18] H. Jiang, Z. Wang, X. Liu , "A two-level approach for solving the inverse kinematics of an extensible soft arm considering viscoelastic behavior," IEEE Rob. Autom. 6127–6133 (2017).
[19] Y. Zhou, J. Li, M. Guo *et al.*, "Modeling and optimization analysis of continuum single-hole surgical robot," Robot **42**(03), 316–324 (2020).
[20] S. Sanan, P. S. Lynn, and S. T. Griffith, "Pneumatic torsional actuators for inflatable robots," J. Mech. Rob. **6**(3), 30–31 (2014).
[21] M. Cianchetti, T. Ranzani, G. Gerboni *et al.*, "Soft robotics technologies to address shortcomings in today's minimally invasive surgery: The STIFF-FLOP approach," Soft Rob. **1**(2), 122–131 (2014).
[22] T. Hou *et al.*, "Design and experiment of a universal two-fingered hand with soft fingertips based on jamming effect," Mech. Mach. Theory **133**, 706 (2019).
[23] Y. Li *et al.*, "Soft robotic grippers based on particle transmission," IEEE/ASME Trans. Mechatron. **24**(3), 969 (2019).
[24] Y. Li, Y. Chen, and Y. Li, "Distributed design of passive particle jamming based soft grippers," in *2018 IEEE International Conference on Soft Robotics (RoboSoft)* (IEEE, 2018), pp. 547–552.
[25] M. Zhu *et al.*, "A fully multi-material three-dimensional printed soft gripper with variable stiffness for robust grasping," Soft Rob. **6**(4), 507–519 (2019).
[26] P. Zheng, "Research on passive flexible variable stiffness joints based on temperature-controlled shape memory alloys," Shandong University, 2020.
[27] E. Brown, N. Rodenberg, J. Amend *et al.*, "Universal robotic gripper based on the jamming of granular material," Proc. Natl. Acad. Sci. U. S. A. **107**(44), 18809–18814 (2010).
[28] Y. Li, Y. Chen *et al.*, "Passive particle jamming and its stiffening of soft robotic grippers," IEEE Trans. Rob. **33**(2), 446–455 (2017).
[29] Y.-J. Kim, S. Cheng *et al.*, "A novel layer jamming mechanism with tunable stiffness capability for minimally invasive surgery," IEEE Trans. Rob. **29**(4), 1031–1042 (2013).
[30] W. Wang and S. H. Ahn, "Shape memory alloy-based soft gripper with variable stiffness for compliant and effective grasping," Soft Rob. **4**, 379–389 (2017).
[31] H. Imamura, K. Kadooka, and M. Taya, "A variable stiffness dielectric elastomer actuator based on electrostatic chucking," Soft Matter **13**(18), 3440–3448 (2017).
[32] Y. Kang, "The development trend of automobile brake," South Agric. Mach. **52**(24), 196–198 (2021).
[33] X. Gao, "Research on wet multi-disc axle brake for mine trackless transporter," Dev. Mech. Manage. **37**(11), 93–95+98 (2022).
[34] X. Hu, Y. Wang, Y. Zhu, M. Song, and L. Guoqiang, "Development and application prospect of electromagnetic brake," Micromotor **47**(04), 71–75 (2019).
[35] L. Zheng, G. Wu, P. Wang *et al.*, "Structural design and experimental study of pneumatic flexible wrist," J. Jilin Inst. Chem. Technol. **38**(11), 67–70 (2021).
[36] D. Geng, G. Sun, L. Qi *et al.*, "Structural optimization design of space joint elastic spherical brake," J. Beihua Univ., Nat. Sci. Ed. **20**(05), 695–700 (2019).
[37] A. N. Jante, *Rubber Engineering* (Chemical Industry Press, Beijing, 2002).
[38] D. Geng, "Bidirectional active bending pneumatic flexible joint and its application in mechanical hand," School of Mechanical Science and Engineering, Jilin University, 2011.
[39] W. Zhong, B. Li, and X. Yan, "Prestressed cylindrical helical spring bending elastic properties research," Mech. Des. **25**, 3 (2008).
[40] Y. Zhang, H. Liu, and D. Wang, *Spring Handbook* (Machinery Industry Press, Beijing, 2008).